

Analytical Model of Six-Pole Axial-Radial Active Magnetic Bearing Based on Flux Density and Segmentation of Magnetic Field

Huangqiu Zhu¹, Zhen Wang¹, and Gai Liu^{2,*}

¹School of Electrical and Information Engineering, Jiangsu University, Zhenjiang 212013, China

²School of Electrical and Control Engineering, Xuzhou University of Technology, Xuzhou, 221018, China

ABSTRACT: To reduce the coupling resulting from structural asymmetry and enhance the load-bearing capacity per unit area, a six-pole axial-radial active magnetic bearing (AR-AMB) has been suggested. To refine the precision of the mathematical model derived from the conventional equivalent magnetic circuit model, a modeling technique that employs flux density and magnetic field segmentation has been proposed. Firstly, the structure and operational principle of the six-pole AR-AMB are introduced. Subsequently, an improved model based on the flux density is established by considering the internal relationship between the iron core and air gap magnetic field in a magnetic bearing with pole shoes. The model addresses issues related to the accurate calculation of fringing magnetic flux and magnetic saturation of core materials while accounting for eddy current effects on suspension force. Finally, the accuracy of the theoretical analysis results has been validated through finite element simulation and experiment, and demonstrated that the rotor based on this model exhibits robust anti-interference capabilities.

1. INTRODUCTION

The primary function of bearings is to provide support for the rotor. With the continuous advancement of modern science and technology, there are increasing demands for clean and pollution-free solutions in fields such as life sciences, while aerospace industries require high-speed and lightweight components [1, 2]. The emergence of magnetic bearings has addressed the issues of friction, pollution, and other problems that arise from the contact between the stator and rotor in conventional mechanical bearings, while also increasing speed [3–5]. Due to the asymmetry of the structure, the relationship between the suspension force and current is nonlinear, and there is a strong coupling between the degrees of freedom. To improve these problems and further increase bearing capacity, a six-pole axial-radial active magnetic bearing (AR-AMB) with a symmetrical structure is proposed [6, 7].

To achieve precise control accuracy in magnetic bearings, the accuracy of the mathematical model of the controlled object is inseparable from advanced control methods [8]. The outcomes obtained through the conventional equivalent magnetic circuit method (EMCM), which relies on simplifying the magnetic field, may not always be accurate [9]. A composite model that alternates between linear and nonlinear models based on the EMCM is proposed in [10], which can provide a control system with the most appropriate mathematical models for suspension force. In [11], the analytical model of a solid-core active magnetic bearing is presented. The model establishes a relationship between magnetic force and effective magnetic resis-

tance based on the traditional electromagnetic circuit method, which is highly applicable in engineering contexts. The analysis in [12] focuses on the examination of leakage effects while disregarding the impact of fringing and eddy current effects on the precision of calculation outcomes. [13] accurately calculates the fringing magnetic flux and leakage coefficient, leading to alignment well with the finite element results. A meticulous analysis model that takes into account the eddy current effects and leakage effects has been proposed [14]. The findings indicate that variations in current can give rise to eddy currents, which in turn can cause a decrease in stiffness and phase lag. An improved magnetic circuit model considering the leakage effects, cross-coupling, and saturation effects is proposed for the performance analysis of three degree of freedom magnetic bearings [15]. Compared with the traditional magnetic circuit model, the permanent magnet bias field, and radial and axial current fields are analyzed. The results show that the improved magnetic circuit model can predict the stiffness more accurately. To streamline the design and analysis of the AMB, a hybrid analysis model has been proposed [16]. This model employs elementary subdomains to model the stator and rotor, while the air gap is represented by equivalent magnetic circuits. The model accounts for both rotor eccentricity and material nonlinearity, resulting in an accurate prediction of the magnetic flux of the AMB. To reduce the calculation time of the magnetic bearing model with pole shoes, it is necessary to establish the internal relationship between the air gap magnetic field and iron core magnetic field while considering the factors that affect the modeling.

* Corresponding author: Gai Liu (lg_just@163.com).

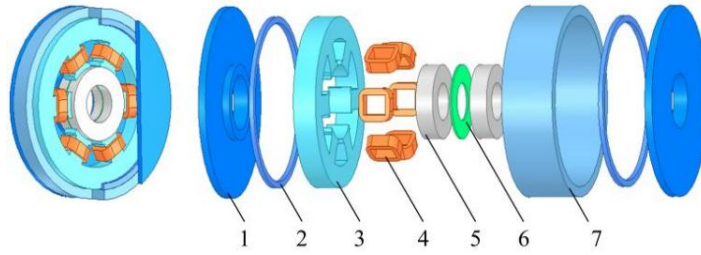


FIGURE 1. The structure diagram of the six-pole AR-AMB. 1. Axial stator. 2. Axial coils. 3. Radial stator. 4. Radial coils. 5. Rotor. 6. Magnetic insulation aluminum ring. 7. Sleeve.

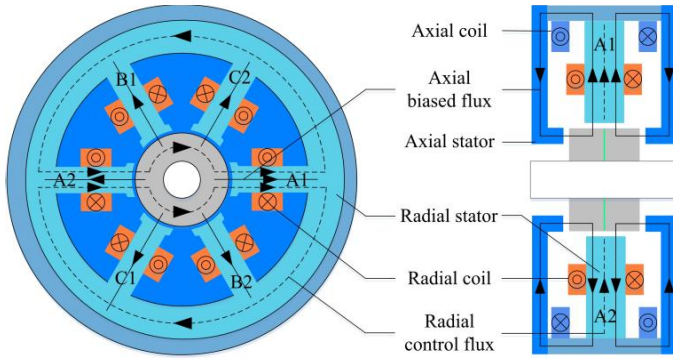


FIGURE 2. The magnetic circuit diagram of the six-pole AR-AMB.

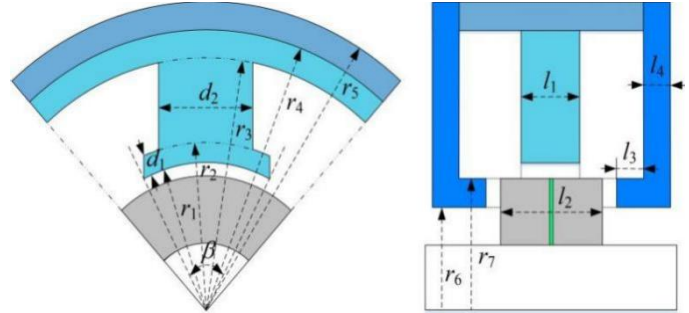


FIGURE 3. The structure parameters of the six-pole AR-AMB.

The primary contributions of this article are as follows. Firstly, it presents an introduction to the operation principle of the six-pole AR-AMB. Subsequently, the air gap magnetic resistance, located directly beneath the magnetic pole’s end face, is calculated based on the flux density, considering the internal relationship between the iron core and air gap magnetic field. The magnetic field is segmented to calculate the air gap magnetic resistance around the magnetic pole end face, and an improved model is established that considers the stator and rotor magnetic resistance. The influence of eddy current effects on the suspension force is considered. Finally, the simulation model and experimental platform are established to validate the precision and superiority of the model.

2. STRUCTURE AND OPERATION PRINCIPLE

The structure diagram of the six-pole AR-AMB is shown in Fig. 1, and it primarily consists of two axial stators, axial coils, a radial stator, etc. The six magnetic poles are wrapped with radial coils, respectively, and the coils on the opposite magnetic poles are in series in reverse to form a phase. The formed three-phase coils are connected in a star mode. The current passing through the three-phase coils is the radial control current, which generates the radial control flux. The axial coil is fixed in the coil cavity of the axial stator by the wire clip, and the formed pair of axial coils is driven by the power amplifier. The current passing through the axial coil is the axial bias current, which generates the axial bias current.

The magnetic circuit of the six-pole AR-AMB is shown in Fig. 2. The bias flux flow is a solid line with arrows, forming a loop among the sleeve, axial stator, axial air gap, rotor, radial

air gap, and radial stator. The control flux flow is a dotted line with arrows, forming a loop among the radial stator, radial air gap, and rotor. In the radial direction, when the rotor is disturbed by the $A1$ direction, the bias flux and control flux are superimposed in the $A2$ direction and canceled in the $A1$ direction. Suspension force along the $A2$ direction is generated to pull the rotor back to the equilibrium position. In the axial direction, the rotor can be stably suspended by changing the magnitude and direction of the current in the axial coils.

3. IMPROVED MODELING

The structural parameters of the six-pole AR-AMB are displayed in Fig. 3, while the specific parameters and constraints are shown in Table 1. The original linearized model can be obtained by using Kirchhoff’s law and refers to the magnetic circuit diagram in Fig. 2 [17].

$$\left\{ \begin{array}{l} F_x = \frac{3\sqrt{6}\mu_0 S_r N_r N_z S_z i_0}{\delta_0^2 (6S_r + S_z)} x + \frac{12\mu_0 S_r N_z^2 S_z^2 i_0^2}{\delta_0^3 (6S_r + S_z)^2} i_x \\ = k_r x + k_{i_r} i_x \\ F_y = \frac{3\sqrt{6}\mu_0 S_r N_r N_z S_z i_0}{\delta_0^2 (6S_r + S_z)} y + \frac{12\mu_0 S_r N_z^2 S_z^2 i_0^2}{\delta_0^3 (6S_r + S_z)^2} i_y \\ = k_r y + k_{i_r} i_y \\ F_z = \frac{432\mu_0 S_r^3 N_z^2 S_z i_0^2}{\delta_0^3 (6S_r + S_z)^3} z + \frac{72\mu_0 S_r N_z^2 S_z i_0}{\delta_0^2 (6S_r + S_z)^2} i_z \\ = k_z z + k_{i_z} i_z \end{array} \right. \quad (1)$$

where μ_0 is the vacuum permeability; S_z and S_r are the axial and radial magnetic pole area; N_r and N_z are the number of turns in the radial coils and the axial coils; i_0 and i_z are the bias current and control current in the axial coils; δ_0 is the air gap lengths.

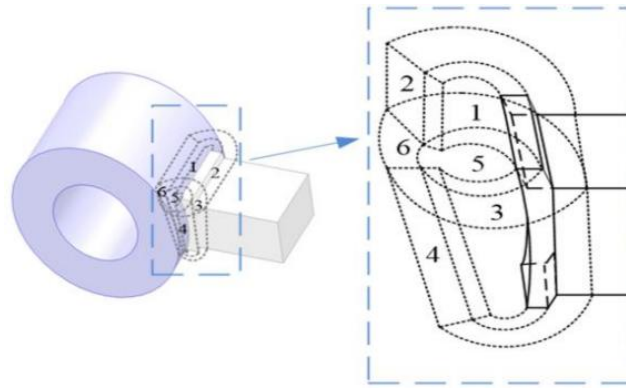


FIGURE 4. The distribution diagram of the edge magnetic flux.

TABLE 1. The design variables of the six-pole AR-AMB.

Symbol (Unit)	Description	Value	range
β (deg)	Pole arc angle	$2\pi/9$	$[\pi/6 \ 5\pi/18]$
d_1 (mm)	Thickness of pole shoe	4	[2 6]
l_1 (mm)	Axial length of magnetic pole	25	[18 32]
d_2 (mm)	Radial width length of magnetic pole	16	[14 20]
r_3 (mm)	Inner radius of stator yoke	50	[46 54]
r_4 (mm)	Outer radius of stator yoke	68	[58 74]
r_5 (mm)	Outer radius of sleeve	76	[66 82]
r_6 (mm)	Inner radius of axial stator	22	[16 28]
r_7 (mm)	Outer radius of axial stator	30	[24 36]
l_2 (mm)	Axial length of rotor	40	[30 50]

3.1. Analytical of Flux Density

To consider the magnetic saturation of the core material, the stator core flux density and air gap flux density are converted by the ratio b of the radial width of the pole column and the arc length of the pole shoe, so that the improved mathematical model based on the flux density is established.

To avoid magnetic saturation and ensure that in a linear region, the working point of the core material is expressed as:

$$\begin{cases} B_{p1} = \frac{1}{2}B_{m1} \\ B_{c1} = B_{m1} - B_{p1} = \frac{1}{2}B_{m1} \end{cases} \quad (2)$$

where B_{p1} , B_{m1} , and B_{c1} are the bias magnetic flux density, maximum magnetic flux density, and control magnetic flux density of the core material, respectively.

Based on the ratio b and according to the principle that the magnetic flux flowing through the stator poles is equal to that flowing through the air gap, it is obtained:

$$\frac{B_{p1}}{B_{p2}} = \frac{B_{c1}}{B_{c2}} = \frac{S_2}{S_1} = \frac{d_2 l_1}{\beta r_1 l_1} = \frac{d_2}{\beta r_1} = \frac{1}{b} \quad (3)$$

where B_{p2} and B_{c2} are the bias magnetic flux density and control magnetic flux density in the radial air gap; S_2 is the area

of the pole shoe; S_1 is the cross-sectional area of the magnetic pole column; d_2 is the radial width of the magnetic pole; l_1 is the axial length of the magnetic pole; β is the pole arc angle; and r_1 is the inner diameter of the magnetic pole.

The current is assumed to be constant while the magnetic field intensity H is constant when the current size and coil shape are determined. Since the air gap permeability G changes positively with the change of the air gap flux density B , the radial air gap permeability based on the flux density should be b times the initial air gap permeability. Since the axial coil is fixed in the middle of the sleeve by wire clips, and the magnetic pole shape of the axial stator is regular without a pole shoe, it is considered that the axial air gap permeability based on the flux density is equal to the initial air gap permeability.

3.2. Calculation of Air Gap Magnetic Permeance

The distribution of the edge magnetic flux is displayed in Fig. 4. The presence of pole shoes and the symmetry of the magnetic poles allow us to divide the edge magnetic flux into six sections using the magnetic field segmentation method. The suspension force is a combination of the edge magnetic flux and main magnetic flux.

Region 1 is roughly equivalent to a 1/4th solid elliptic cylinder, and we can obtain the permeance value for it.

$$G_1 = \frac{2\mu_0 l_1}{\pi} \ln \left(1 + \frac{\pi d_1}{2\delta_r} \right) \quad (4)$$

Region 2 is a quarter hollow cylinder with permeance obtained from:

$$G_2 = \frac{2\mu_0 l_1}{\pi} \ln \left(1 + \frac{m}{\delta_r + d_1} \right) \quad (5)$$

where m is the length of the edge magnetic flux distributed radially along the magnetic pole.

Similarly, the permeance of other regions can be obtained:

$$G_3 = \frac{2\mu_0 \beta r_1}{\pi} \ln \left(1 + \frac{\pi d_1}{2\delta_r} \right) \quad (6)$$

$$G_4 = \frac{2\mu_0 d_2}{\pi} \ln \left(1 + \frac{m}{\delta_r + d_1} \right) \quad (7)$$

$$G_5 = \frac{\mu_0 \pi \delta(\theta)}{9.83} \quad (8)$$

$$G_6 = \mu_0 \delta(\omega) \quad (9)$$

where θ is the angle between the magnetic pole $A1$ and the positive direction of the x axis.

The total magnetic permeance of an air gap can be calculated by adding the edge permeance and the main permeance under the magnetic pole end face in parallel. Taking the $A1$ direction as an example:

$$G_{sA1} = bG_{A1} + 2(G_1 + G_2 + G_3 + G_4) + 4(G_5 + G_6) \quad (10)$$

Similarly, the total magnetic permeance of the air gap in the $z1$ direction can be obtained:

$$G_{sz1} = G_{z1} + (G_7 + G_8) \quad (11)$$

where

$$G_7 = 2\mu_0 r_7 \ln \left(1 + \frac{\pi m}{\delta_z} \right) \quad (12)$$

$$G_8 = 4\mu_0 r_6 \ln \left(1 + \frac{\pi m}{2\delta_z} \right) \quad (13)$$

3.3. Calculation of Stator and Rotor Magnetic Permeance

The rotor magnetic permeance calculation area is a hollow cylinder, and its magnetic permeance is:

$$G_{r1} = \frac{\mu_0 \mu_r l_2}{\pi} \ln \frac{r_2}{r_1} \quad (14)$$

where r_1 and r_2 are the inner and outer diameters of the rotor, and μ_r is the relative magnetic permeability of the core.

Similarly, the magnetic permeance of the radial magnetic pole, radial yoke, axial stator, and 1/2 sleeve can be obtained:

$$G_{r2} = \frac{\mu_0 \mu_r \beta r_1 l_1}{d_1} + \frac{\mu_0 \mu_r d_2 l_1}{r_3 - r_2} \quad (15)$$

$$G_{r3} = \frac{\mu_0 \mu_r l_1}{2\pi} \ln \frac{r_4}{r_3} \quad (16)$$

$$G_{z1} = \frac{\mu_0 \mu_r \pi (r_7^2 - r_6^2)}{l_3} + \frac{\mu_0 \mu_r l_4}{2\pi} \ln \frac{r_5}{r_6} \quad (17)$$

$$G_{z2} = \frac{\mu_0 \mu_r \pi (r_5^2 - r_4^2)}{\frac{l_2}{2} + \delta_z + l_3} \quad (18)$$

where l_3 is the axial length of the axial stator pole shoe, and l_4 is the axial length of the axial stator column.

3.4. Calculation of Suspension Force and Stiffness

According to the relationship between suspension force and air gap magnetic flux:

$$F_n = \frac{\Phi_n^2}{2\mu_0 S} \quad (19)$$

where $n = A1, A2, B1, B2, C1, C2, z1, z2$, S is the cross-sectional area projected onto the rotor by the magnetic pole.

The effective reluctance can be obtained by inverting the permeance, and the magnetic circuit is illustrated in Fig. 5. The magnetic flux expressions can then be obtained.

$$\left\{ \begin{array}{l} \Phi_{z1} = \frac{N_z(i_0 - i_z)}{R_{sr} + R_z + R_{sz1}}, \quad \Phi_{z2} = \frac{N_z(i_0 + i_z)}{R_{sr} + R_z + R_{sz2}} \\ \Phi_{A1} = \frac{N_z(i_0 - i_z)}{R_{sr} + R_z + R_{sz1}} \cdot \frac{R_{sr}}{R_{sA1}} + \frac{N_z(i_0 + i_z)}{R_{sr} + R_z + R_{sz2}} \\ \quad \cdot \frac{R_{sr}}{R_{sA1}} + \frac{N_r i_a}{R_{sA1} + R_r} \\ \Phi_{A2} = \frac{N_z(i_0 - i_z)}{R_{sr} + R_z + R_{sz1}} \cdot \frac{R_{sr}}{R_{sA2}} + \frac{N_z(i_0 + i_z)}{R_{sr} + R_z + R_{sz2}} \\ \quad \cdot \frac{R_{sr}}{R_{sA2}} - \frac{N_r i_a}{R_{sA2} + R_r} \\ \Phi_{B1} = \frac{N_z(i_0 - i_z)}{R_{sr} + R_z + R_{sz1}} \cdot \frac{R_{sr}}{R_{sB1}} + \frac{N_z(i_0 + i_z)}{R_{sr} + R_z + R_{sz2}} \\ \quad \cdot \frac{R_{sr}}{R_{sB1}} + \frac{N_r i_b}{R_{sB1} + R_r} \\ \Phi_{B2} = \frac{N_z(i_0 - i_z)}{R_{sr} + R_z + R_{sz1}} \cdot \frac{R_{sr}}{R_{sB2}} + \frac{N_z(i_0 + i_z)}{R_{sr} + R_z + R_{sz2}} \\ \quad \cdot \frac{R_{sr}}{R_{sB2}} - \frac{N_r i_b}{R_{sB2} + R_r} \\ \Phi_{C1} = \frac{N_z(i_0 - i_z)}{R_{sr} + R_z + R_{sz1}} \cdot \frac{R_{sr}}{R_{sC1}} + \frac{N_z(i_0 + i_z)}{R_{sr} + R_z + R_{sz2}} \\ \quad \cdot \frac{R_{sr}}{R_{sC1}} + \frac{N_r i_c}{R_{sC1} + R_r} \\ \Phi_{C2} = \frac{N_z(i_0 - i_z)}{R_{sr} + R_z + R_{sz1}} \cdot \frac{R_{sr}}{R_{sC2}} + \frac{N_z(i_0 + i_z)}{R_{sr} + R_z + R_{sz2}} \\ \quad \cdot \frac{R_{sr}}{R_{sC2}} - \frac{N_r i_c}{R_{sC2} + R_r} \end{array} \right. \quad (20)$$

where $R_{sr} = R_{sA1} // R_{sA2} // R_{sB1} // R_{sB2} // R_{sC1} // R_{sC2}$, $R_z = R_{z1} + R_{z2} + R_{r1}$, $R_r = R_{r1}/2 + R_{r2} + R_{r3}/2$; Φ_{z1} and Φ_{z2} are the right and left axial air gap magnetic flux; N_r is the number of turns in the radial coils; Φ_{ij} ($i = A, B, C, j = 1, 2$) are the magnetic flux of the radial air gap; and i_k ($k = a, b, c$) is the three-phase control current.

The suspension force at each air gap is decomposed into x -, y - and z -direction and superimposed. The suspension force expression is as follows:

$$\left\{ \begin{array}{l} F_x = F_{A1} + \frac{1}{2}(F_{B2} + F_{C2}) - F_{A2} - \frac{1}{2}(F_{B1} + F_{C1}) \\ F_y = \frac{\sqrt{3}}{2}(F_{B1} + F_{C2}) - \frac{\sqrt{3}}{2}(F_{B2} + F_{C1}) \\ F_z = F_{z1} - F_{z2} \end{array} \right. \quad (21)$$

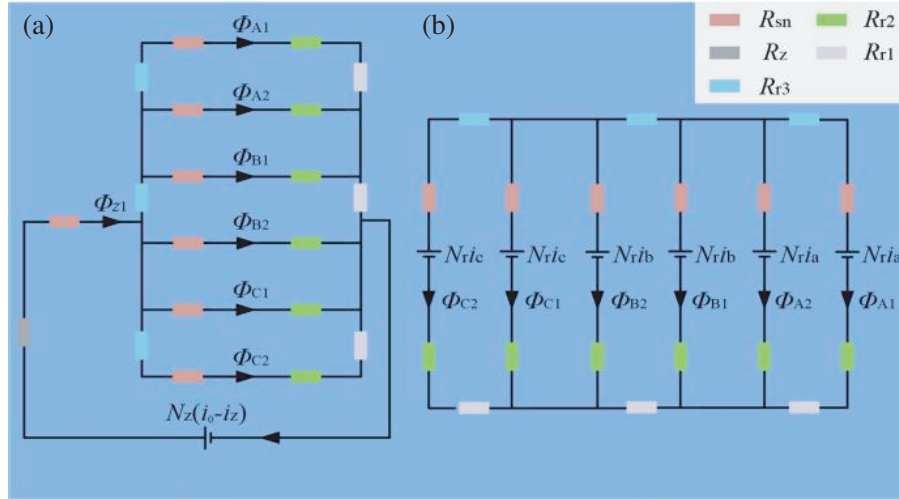


FIGURE 5. The magnetic circuit diagram. (a) Axial direction. (b) Radial direction.

The axial and radial displacement and current stiffness coefficients of the six-pole AR-AMB are obtained:

$$\begin{cases} F_x = \frac{228N_z^2 R_{sr}^2 i_0^2 R_8}{25\delta_0^2 (R_{sr} + R_z + R_7)^2} x + \frac{3\sqrt{6}N_r N_z R_{sr} i_0 R_8}{\mu_0 S_r (R_r + R_8)(R_{sr} + R_z + R_7)^2} i_x \\ F_y = \frac{228N_z^2 R_{sr}^2 i_0^2 R_8}{25\delta_0^2 (R_{sr} + R_z + R_7)^2} y + \frac{3\sqrt{6}N_r N_z R_{sr} i_0 R_8}{\mu_0 S_r (R_r + R_8)(R_{sr} + R_z + R_7)^2} i_y \\ F_z = \frac{2N_z^2 i_0^2 R_7^2}{\delta_0^2 (R_{sr} + R_z + R_7)^3} z + \frac{2N_z^2 i_0}{\mu_0 S_z (R_{sr} + R_z + R_7)^2} i_z \end{cases} \quad (22)$$

where

$$R_7 = \frac{1}{\frac{1}{R_5} + \frac{1}{R_6} + \frac{\mu_0 S_z}{\delta_0}} \quad (23)$$

$$R_8 = 2\frac{1}{R_1} + 2\frac{1}{R_2} + 2\frac{1}{R_3} + 2\frac{1}{R_4} + \frac{19\mu_0 S_r}{25\delta_0} \quad (24)$$

3.5. Analyzing Eddy Current Effect

The iron core material is made of silicon steel sheets with a thickness of 0.35 mm, which can suppress the eddy current effects caused by the rotor rotating and cutting the magnetic field lines of the air gap field. But when the rotor vibration frequency is high, it has a significant impact on the air gap magnetic field. The air gap magnetic field distribution no longer uniform is made by the generated eddy current field, resulting in a smaller suspension force than that at rest. The faster the rotation speed is, the more obvious this phenomenon is [18].

The dynamic relative permeability is introduced, and the influence of eddy current on the air gap magnetic field is equivalent to the decrease of relative permeability of the core material as the frequency increases. The expression is:

$$\mu_{df} = \mu_d \frac{\tanh(\sqrt{j\omega\sigma\mu_0\mu_d}\frac{d}{2})}{\sqrt{j\omega\sigma\mu_0\mu_d}\frac{d}{2}} \quad (25)$$

where ω is the frequency of magnetic flux change, σ the electrical conductivity of the core material, μ_d the static relative

magnetic permeability, and d the thickness of the silicon steel sheet.

By substituting Equation (25) into Equations (14) ~ (21), the influence of eddy current effects on the suspension force can be considered.

4. SIMULATION VALIDATIONS

Since the magnetic bearing is symmetrical in structure, and the stiffness coefficients in the x - and y -direction are consistent, the simulation studies in the x direction are conducted in the radial direction. The simulation results of air gap magnetic density and current stiffness based on the original model and the improved model are analyzed.

4.1. Air Gap Magnetic Density

The distribution of the air gap magnetic density is shown in Fig. 6 and Fig. 7. When there is a control current, the air gap magnetic densities of the original model and the improved model in the z direction are about 0.80 T and 0.84 T, while in the A1 direction they are about 0.79 T and 0.86 T, and in the A2 direction about 0.06 T and 0.09 T, respectively. The control flux and bias flux are superimposed in the A1 direction and canceled in the A2 direction. This is consistent with the theoretical analysis in Section 2. Based on the above analysis, the improved model considers magnetic density more fully than the original model.

4.2. Current Stiffness Characteristic

The curves of current stiffness characteristics are shown in Fig. 8. When the rotor is near the equilibrium position, that is, the change of suspension force on current when the displacement is zero, the current stiffness of the original model in the x direction is about 173.15 N/A while that of the improved model is 189.43 N/A, which means that it is 9.4% higher than the original model. At the same time, the improved model has improved

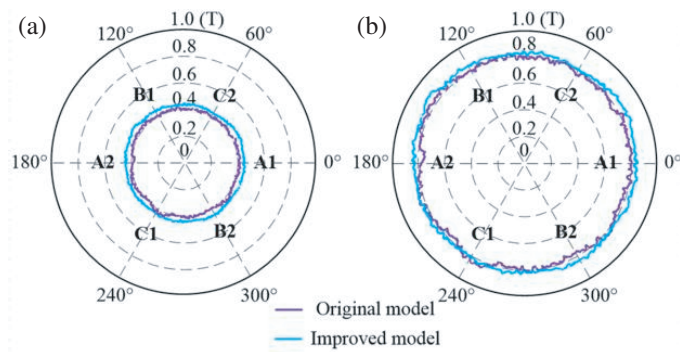


FIGURE 6. The distribution diagrams of the magnetic flux density in the z direction. (a) Without control current. (b) With maximum control current.

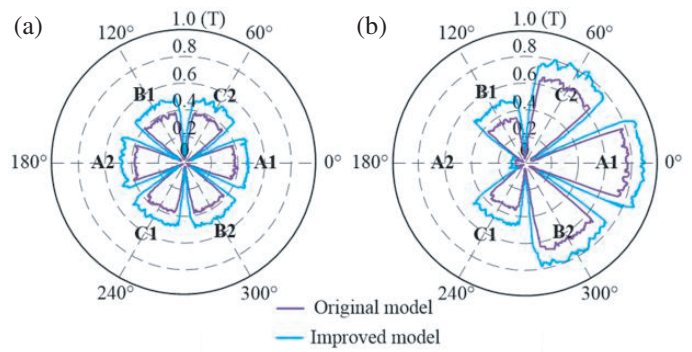


FIGURE 7. The distribution diagrams of the magnetic flux density in the x direction. (a) Without control current. (b) With maximum control current.

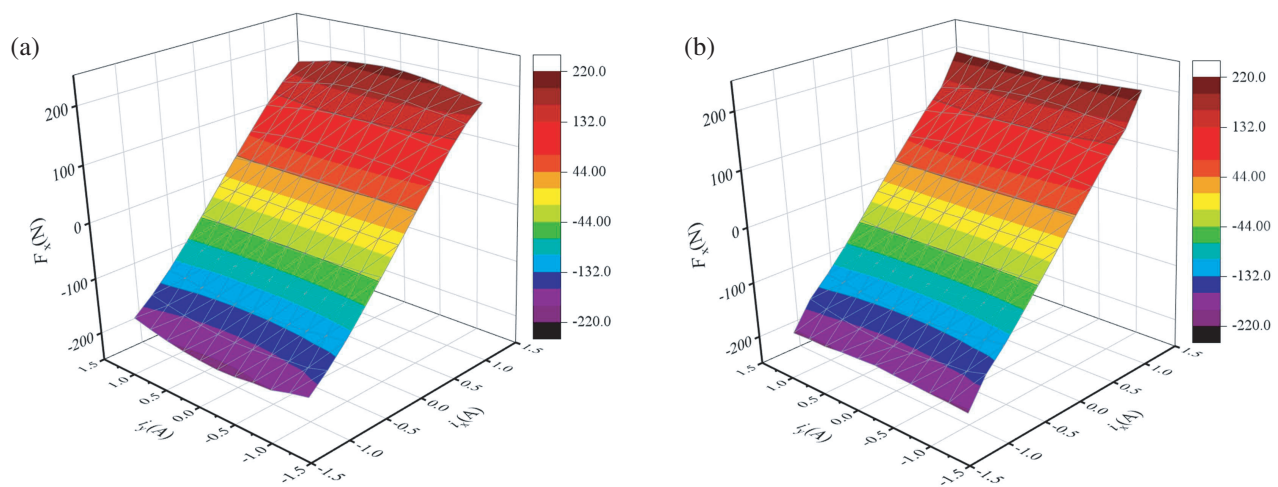


FIGURE 8. The curves of current stiffness characteristic. (a) Original model. (b) Improved model.

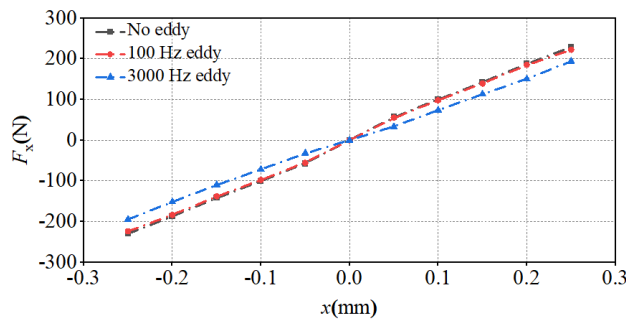


FIGURE 9. The curves of suspension force depending on rotor displacement.

linearity compared with the original model. This indicates that the improved model can generate greater suspension force with the same control current.

4.3. Eddy Current Effect

The influence of the eddy current effects on the relationship between suspension and rotor displacement is shown in Fig. 9. When the eddy current effect is not taken into account, the maximum suspension force in the x direction meets the radial sus-

pension force requirement of 200 N, reaching 230 N. When the rotor vibration frequency is 100 Hz, the suspension force attenuation is around 1.43%, due to the characteristics of the hyperbolic tangent function in Equation (28). At low rotor vibration frequencies, the eddy current effect has almost no impact on the suspension force as the relative permeability of the iron core material remains unchanged. However, at a vibration frequency of 3000 Hz, the suspension force attenuation is around 14.61%, and the eddy current effect reduces the suspension force. As the rotor vibration frequency increases, the

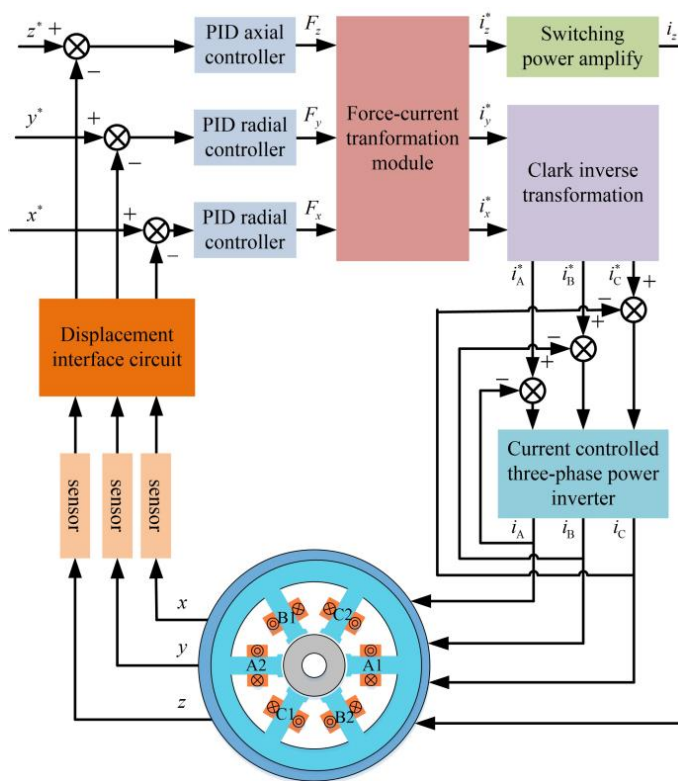


FIGURE 10. The control system of the six-pole AR-AMB.

suspension force attenuation gradually rises, which aligns with the theoretical analysis in Section 3.

5. EXPERIMENTAL VALIDATIONS

5.1. Experimental Platform and Control System

To verify the accuracy and superiority of the proposed improved model, the control system is shown in Fig. 10. The constructed test platform is shown in Fig. 11, mainly including the six-pole AR-AMB, radial power drive board, DSP board, etc. The stiffnesses, floating and disturbance validation tests are carried out.

5.2. Performance Tests

The waveforms of the floating experiment are shown in Fig. 12. When the coil is not energized, the rotor is docked on the auxiliary bearing at the lower end due to gravity, and at 0.2 s, the coil is energized. The rotor returns to the equilibrium position after about 38 ms and 21 ms in the x direction based on the original model and the improved model, respectively, indicating that the improved model has a short response time and good floating performance. The waveforms of the anti-interference experiment are shown in Fig. 13. When an external disturbance force of 50 N is applied in the x direction, the displacements in the x direction are 26 μm and 18 μm , and the corresponding recovery times are 168 ms and 115 ms based on the original model and improved model, respectively, indicating that the improved model has strong anti-interference ability, which is consistent with the simulation results in Section 4.

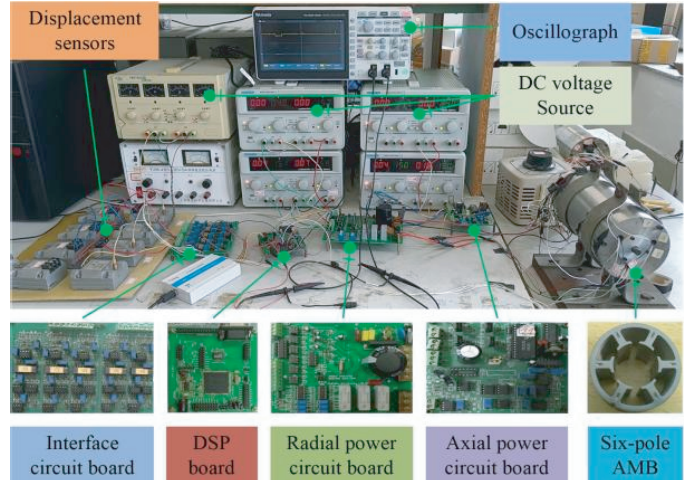


FIGURE 11. The experimental platform of the six-pole AR-AMB.

5.3. Stiffness Tests

Taking the current stiffness test process as an example, PID is adjusted so that the rotor can overcome gravity and hover stably in the equilibrium position; then constant load is applied to the rotor in the x direction to make the rotor deviate from the equilibrium position; control current i_x is adjusted so that the rotor can overcome external disturbance force and return to the equilibrium position. At this time, the load applied is the suspension force F_x generated by the control current i_x . The amount of loads imposed on the rotor by multiple groups and the corresponding control current i_x which can make the rotor return to the equilibrium position are recorded, and the relationship between the suspension force F_x and control current i_x is obtained.

The relationship between the suspension force and control current in the x direction is shown in Fig. 14(a). The original model has a maximum error of 10.7% between the suspension force calculated and the simulation and experiment values. In contrast, the improved model has an error of less than 3%. This is because the original model considers the air gap magnetic field density to be equal to the iron core magnetic field density. The relationship between the suspension force and the rotor displacement in the x direction is shown in Fig. 14(b). The original model has a maximum error of 9.6% between the suspension force calculated and simulation and experiment values. The improved model, however, has an error of less than 2%. The error increases as the rotor displacement increases because the original model does not consider the influence of other parts of reluctance on the magnetic circuit. The stiffness characteris-

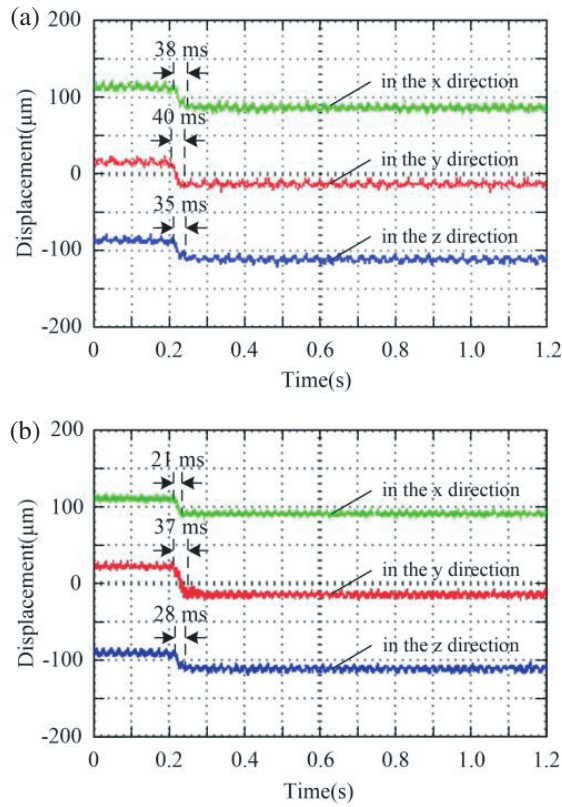


FIGURE 12. The waveforms of the floating experiment. (a) Original model. (b) Improved model.

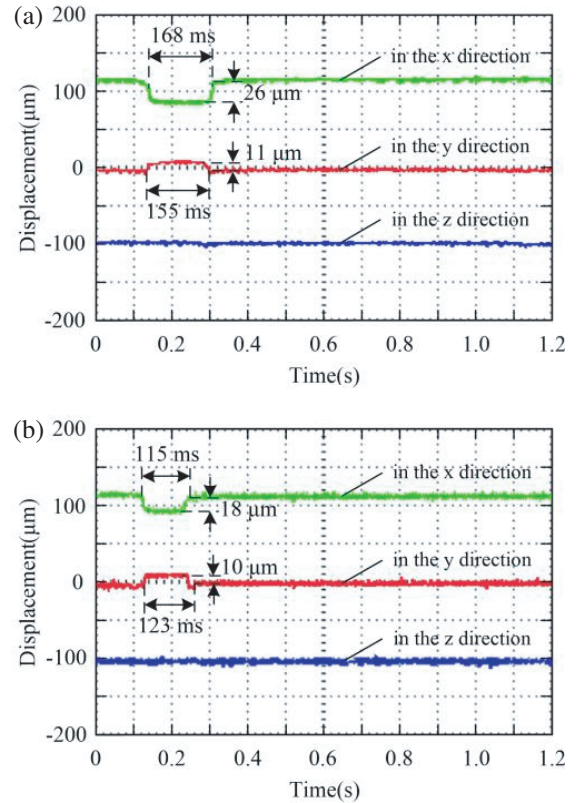


FIGURE 13. The waveforms of the anti-interference experiment. (a) Original model. (b) Improved model.

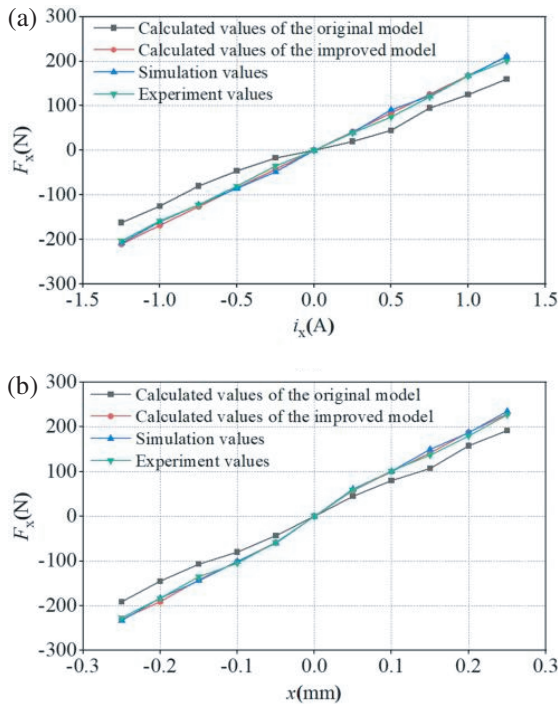


FIGURE 14. The curves in the x direction. (a) Suspension force and control current. (b) Suspension force and rotor displacement.

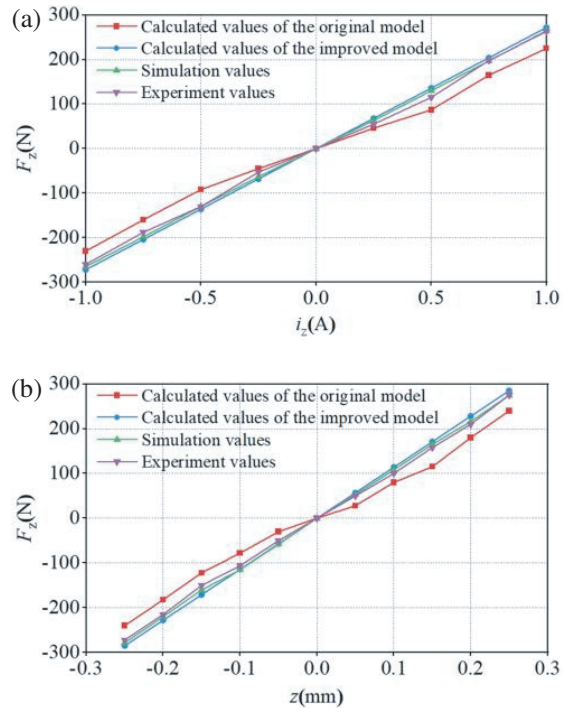


FIGURE 15. The curves in the z direction. (a) Suspension force and control current. (b) Suspension force and rotor displacement.

tics in the z direction are shown in Fig. 15, which is consistent with the analysis conducted previously. In conclusion, the improved model is a better approximation of the simulation and experiment values than the original model.

6. CONCLUSION

In the paper, an improved modeling method for sixpole AR-AMB based on the flux density and segmentation of the magnetic field is proposed. Through the internal relationship between the iron core and air gap magnetic field, and the segmentation of different regions of the magnetic field, the main magnetic flux and fringing magnetic flux are accurately calculated. The dynamic relative permeability is introduced to consider the influence of eddy current effects on the suspension force. The simulated and experimental results show that the calculation results of the improved model are basically consistent with the simulated and experimental results. Compared with the original model, the current stiffness is increased by 9.4%, and the displacement stiffness is increased by 16.34%. The modeling results are more accurate, and the magnetic density is considered more fully. The control system based on the improved model has stronger anti-interference performance, which is beneficial for designing high-performance controllers in the future. The modeling method based on the flux density and segmentation of magnetic field has certain applicability and superiority for considering the influence of the eddy current effects, and the accurate calculation of magnetic flux, especially for calculating air gap magnetic flux with pole shoe magnetic bearings.

ACKNOWLEDGEMENT

This project was sponsored in part by National Natural Science Foundational of China (62273168).

REFERENCES

- [1] Zheng, Y., N. Mo, Y. Zhou, and Z. Shi, "Unbalance compensation and automatic balance of active magnetic bearing rotor system by using iterative learning control," *IEEE Access*, Vol. 7, 122 613–122 625, 2019.
- [2] Le, Q. Y. and W. G. Zhu, "Design and analysis of a new five-degree-of-freedom DC hybrid magnetic bearing," *IEEE Transactions on Applied Superconductivity*, Vol. 31, No. 8, 1–4, 2021.
- [3] Wu, M., H. Zhu, H. Zhang, and W. Zhang, "Modeling and multi-level design optimization of an AC-DC three-degree-of-freedom hybrid magnetic bearing," *IEEE Transactions on Industrial Electronics*, Vol. 70, No. 1, 233–242, 2023.
- [4] Usman, I.-U.-R., M. Paone, K. Smeds, and X. Lu, "Radially biased axial magnetic bearings/motors for precision rotary-axial spindles," *IEEE/ASME Transactions on Mechatronics*, Vol. 16, No. 3, 411–420, 2011.
- [5] Jiang, D., T. Li, Z. Hu, and H. Sun, "Novel topologies of power electronics converter as active magnetic bearing drive," *IEEE Transactions on Industrial Electronics*, Vol. 67, No. 2, 950–959, 2020.
- [6] Sun, J. and H. Zhu, "Self-sensing technology of rotor displacement for six-pole radial active magnetic bearing using improved quantum particle swarm optimized cubature kalman filter," *IEEE Journal of Emerging and Selected Topics in Power Electronics*, Vol. 10, No. 3, 2881–2889, 2022.
- [7] Liu, G., Y. Wu, J. D. Huang, *et al.*, "Rotor displacement self-detection of six-pole outer rotor radial hybrid magnetic bearing," *Journal of Xuzhou Institute of Technology*, Vol. 39, No. 1, 1–12, 2024.
- [8] Loussert, G. and J.-D. Alzingre, "A magnetic and mechanical force model for the design of an archimedean spiral flexure bearing for a linear direct-drive electromagnetic actuator," *IEEE/ASME Transactions on Mechatronics*, Vol. 24, No. 4, 1617–1627, 2019.
- [9] Han, B., S. Zheng, H. Li, and Q. Liu, "Weight-reduction design based on integrated radial-axial magnetic bearing of a large-scale MSCMG for space station application," *IEEE Transactions on Industrial Electronics*, Vol. 64, No. 3, 2205–2214, 2017.
- [10] Zhang, W., H. Zhu, Z. Yang, X. Sun, and Y. Yuan, "Nonlinear model analysis and "switching model" of AC-DC three-degree-of-freedom hybrid magnetic bearing," *IEEE/ASME Transactions on Mechatronics*, Vol. 21, No. 2, 1102–1115, 2016.
- [11] Zhou, L. and L. Li, "Modeling and identification of a solid-core active magnetic bearing including eddy currents," *IEEE/ASME Transactions on Mechatronics*, Vol. 21, No. 6, 2784–2792, 2016.
- [12] Wang, H., Z. Wu, K. Liu, J. Wei, and H. Hu, "Modeling and control strategies of a novel axial hybrid magnetic bearing for flywheel energy storage system," *IEEE/ASME Transactions on Mechatronics*, Vol. 27, No. 5, 3819–3829, 2022.
- [13] Wang, H., K. Liu, J. Wei, and H. Hu, "Analytical modeling of air gap magnetic fields and bearing force of a novel hybrid magnetic thrust bearing," *IEEE Transactions on Magnetics*, Vol. 57, No. 10, 1–7, 2021.
- [14] Le, Y., J. Sun, and B. Han, "Modeling and design of 3-DOF magnetic bearing for high-speed motor including eddy-current effects and leakage effects," *IEEE Transactions on Industrial Electronics*, Vol. 63, No. 6, 3656–3665, 2016.
- [15] Zhong, Y., L. Wu, X. Huang, Y. Fang, and J. Zhang, "An improved magnetic circuit model of a 3-DOF magnetic bearing considering leakage and cross-coupling effects," *IEEE Transactions on Magnetics*, Vol. 53, No. 11, 1–6, 2017.
- [16] Cao, Z., Y. Huang, B. Guo, F. Peng, J. Dong, and A. Hemeida, "A novel hybrid analytical model of active magnetic bearing considering rotor eccentricity and local saturation effect," *IEEE Transactions on Industrial Electronics*, Vol. 69, No. 7, 7151–7160, 2022.
- [17] Zhu, H. and S. Wang, "Electromagnetic characteristics analysis and experiment study of six-pole radial-axial active magnetic bearing," *Proceedings of the CSEE*, Vol. 40, No. 5, 1653–1663, 2020.
- [18] Le, Y., J. Fang, and K. Wang, "Design and optimization of a radial magnetic bearing for high-speed motor with flexible rotor," *IEEE Transactions on Magnetics*, Vol. 51, No. 6, 1–13, 2015.